Post-treatments on carbon xerogels to improve their performance as negative electrodes of Na-ion batteries

Berke Karaman[1], Hélène Tonnoir[1,2], Da Huo[2], Jimena Castro Gutiérrez[3], Bryan Carré[1], Alexandre F. Léonard[4], Marion Bermont[2], Zoé Deckers[1], Alain Celzard[3,5], Vanessa Fierro[3], Carine Davoisne[2], Raphaël Janot[2], Nathalie Job[1,*]

[1]*Department of Chemical Engineering - NCE (Nanomaterials, Catalysis, Electrochemistry), University of Liège, 4000 Liège, Belgium*
[2]*Laboratoire de Réactivité et Chimie des Solides - LRCS, UMR7314 CNRS, Université de Picardie Jules Verne, Amiens, France*
[3]*Université de Lorraine, CNRS, Institut Jean Lamour - IJL, 88000 Épinal, France*
[4]*Department of Chemical Engineering - CARPOR, University of Liège, 4000 Liège, Belgium*
[5]*Institut Universitaire de France - IUF, 75231 Paris, France*
*(*corresponding author: nathalie.job@uliege.be)*

Keywords: Hard carbon, carbon xerogels, CO_2 activation, Na-ion batteries

Abstract

A carbon xerogel (CX) with ~2 µm nodules was synthesized *via* polycondensation of resorcinol with formaldehyde in water, followed by pyrolysis at 800 °C. The resulting sample underwent surface treatments using Chemical Vapor Deposition (CVD) and/or CO_2 activation in order to mask the micropores with a secondary carbon layer or develop additional micropores, respectively. This strategy aimed at understanding the impact of surface modification and closed micropores on the performance of hard carbons as negative electrode materials for Na-ion battery. On the one hand, the coating deposited by CVD was found to display more graphitic-like domains and to close the CX microporosity, leading to enhanced Initial Coulombic Efficiency (ICE) and reversible capacity. On the other hand, due to its very high accessible surface area, the activated sample showed very low ICE (18%) and reversible capacity (62 mAh g^{-1}). However, once the activated sample was covered with a secondary carbon layer by CVD, the capacity reached 294 mAh g^{-1} with a high ICE of around 88%, and an enhanced insertion plateau at low voltage was observed. Additionally, this activated-coated sample showed a high-rate capability and much greater stability than the other samples upon cycling. Such surface treatments provide an effective strategy for both understanding the impact of hard carbon surface properties on Na storage and optimizing their performance for negative electrodes in Na-ion batteries.

* Corresponding author: Nathalie.Job@uliege.be

1. Introduction

Na-ion batteries (NIBs) are promising candidates to overtake Li-ion batteries (LIBs) in view of reducing the dependence over critical materials [1-4]. Indeed, not only do they replace Li by widely available Na, but they also use Al instead of Cu as current collector at the negative electrode and do not need costly metals such as Co. However, NIBs are not yet very popular compared with LIBs, due to their lower power and energy density [5]. To increase the total amount of energy delivered by NIBs per weight/volume, improving the materials of the negative electrode is the crucial step. Since graphite, which is widely used in LIBs, intercalates Na^+ quite poorly [6, 7], it is usually replaced in NIBs by hard carbons, *i.e.* disordered carbons usually produced by pyrolysis of various precursors, generally oxygen-rich molecules or polymers. These materials can reach capacities of up to 320 mAh g^{-1} [8, 9], making them suitable for practical applications, though further improvement is still needed. Additionally, electrolyte decomposition and formation of Solid Electrolyte Interphase (SEI) on their surface often leads to low Initial Coulombic Efficiency (ICE), since hard carbons typically have high specific surface areas [10, 11]. Therefore, the main challenge for these materials is to improve both their capacity and their ICE.

Numerous methods have been suggested in the literature to overcome both issues. Capacity has been increased through defect tailoring and precursor modification [12], and formation of curvatures by heteroatom doping [13] or even introduction of catalysts [14]. Regardless of the strategy, all studies underline the crucial role of carbon surface properties, especially their specific surface area, on the ICE. In this context, it is important to note that a better understanding of the actual electrode surface is needed. Indeed, in the literature [15], the ICE observed in half-cell is quite often linked to the specific surface area measured by gas sorption (*i.e.* the BET surface area, A_{BET}), which, at first sight, makes sense since the larger the surface area, the more SEI can be formed at the first cycle; this relationship indeed proves true for some carbons [15]. However, our recent work showed that materials with similar A_{BET} values can display drastic differences in ICE [16]. One possible explanation could be that, although the whole carbon surface is accessible to gases such as N_2, H_2 or CO_2 in adsorption experiments, this may not be the case for the liquid electrolyte in the final cell. As a result, adsorption data do not correlate with the final electrochemical performance. Additionally, the mechanism of Na storage in hard carbons remains unclear, even though the slope region is ascribed to ion adsorption on carbons defects and Na^+ intercalation between graphene layers, while the low-voltage plateau region is associated with cluster storage in micropores [17-20].

In turn, open micropores are generally the main contributors to the specific surface area measured by adsorption. Given the above information, the ideal carbon material would present a large surface area accessible to Na^+ ions but not accessible to the electrolyte. This highlights the need for a systematic study of the impact of specific surface area on both the ICE and the capacity of hard carbon electrodes, using model carbon materials such as carbon xerogels and employing surface modifications strategies to control the area available for SEI formation.

Carbon xerogels (CXs) are usually synthesized by evaporative drying and pyrolysis of organic gels (*e.g.* aqueous resorcinol-formaldehyde gels) [21]. Their structure consists of interconnected, microporous spherical nodules, whose size can be tailored from a few nm to a few µm depending on the composition of the gel precursor solution. As a result, their meso/macroporous texture, which corresponds to the voids between the microporous nodules, can be adjusted from a few nm to a few µm as well. Mesoporous CXs were used in a previous work [11] as negative electrode materials for NIBs, but their ICE was low due to their high accessible specific surface area (~600 m^2 g^{-1}). However, their reversible capacity could reach relatively high values, around 200 mAh g^{-1} (at 37.2 mA g^{-1}). In order to improve CX performance, the impact of the nodule size has also been investigated in our previous study: it has been reported that carbon xerogels with large nodules (1-2 µm) pyrolyzed at low temperature (800 °C) can lead to quite good reversible capacity (248 mAh g^{-1}) and very high ICE (80%) [16]. This high ICE value was ascribed to the inaccessibility of the electrolyte to the micropores within the nodules, whereas Na^+ ions can be stored within these micropores. Masking the micropores by depositing a secondary carbon layer by Chemical Vapor Deposition (CVD) led to even higher reversible capacity (298 mAh g^{-1}) and ICE (84%). Therefore, surface accessibility of the electrolyte seems to be the key to the high performance of CXs as NIB electrode materials.

To better understand the impact of the CX surface on electrochemical properties, the microporosity of CXs can be tuned in various ways. Firstly, as demonstrated in our previous work [16], CVD is an efficient method to close open micropores by depositing a secondary carbon layer on the outer surface of the nodules, thus hampering the access of electrolyte to the inner surface of the carbon nodules. Secondly, CO_2 activation can be used to increase the total surface area by forming new micropores [22], which can be seen as the exact opposite of what is typically required for an ideal electrode material. However, the combination of these two procedures (*i.e.* CO_2 activation followed by CVD coating) can be beneficial as it can lead to a large volume of closed micropores, which is desired to obtain a large volume accessible to Na^+

while restricting electrolyte penetration. Method of introduction closed pores are being tried recently in literature rather with pre-pyrolization procedures such as precursor linking [23], pre-oxidation[24] or protonation-mediated strategy [25].

In this approach, post treatments of carbon xerogel will be done by CO_2 activation to enhance microporosity and CVD carbon coating would limit its accessibility to the electrolyte. Consequently, this strategy would enable the development of a CX with enhanced capacity and high ICE. Moreover, from a fundamental perspective, it could provide new insights into the relationship between the specific surface area and the material performance in NIB electrode.

In this study, which directly follows our previous work [16], we aim at understanding better the relationship between the specific surface area of hard carbons and their performances as NIB negative electrode materials. To this end, a CX with a large nodule size (~2.0 µm) and a standard specific surface area (645 $m^2 g^{-1}$) was activated by CO_2 to enhance microporosity, and thus increase the total specific surface area. The micropores were then masked with a secondary carbon layer by CVD to reduce the accessibility of the electrolyte to the nodules' inner surface. The materials, obtained after activation and after CVD coating, were characterized using various physicochemical methods and their electrochemical performance in NIB half-cells was determined. The results were compared with those obtained previously with pristine CX and the same material after CVD treatment without any activation. The results highlight the impact of both post-treatments on the electrochemical performance of these hard carbons as NIB negative electrode materials and help determining what surface has to be considered as descriptor toward high ICE values.

2. Experimental

2.1. Synthesis of the carbon xerogel

The pristine carbon xerogel (CX) was prepared following a procedure described in a previous study [26]. First, a 35 wt.% aqueous solution of resorcinol (R, Merck) was prepared in a sealable glass flask. A 37 wt.% solution of formaldehyde (F) in water was then added to the mixture with a resorcinol/formaldehyde molar ratio of 0.5. The dilution ratio *D*, *i.e.* the water (including the water in F)/reactants molar ratio, was equal to 5.7. Note that, normally, sodium carbonate is added as a basification agent to regulate the nodule size. However, for this study, no sodium carbonate was added in order to produce a gel under low pH conditions, so as to obtain a material with large nodule size [26, 16]. The obtained mixture was stirred with a

magnetic stirrer for 1 h. After mixing, the sealed glass flask was put in an oven at 85 °C for 72 h for gelation and aging. Finally, the container was opened and placed in a vacuum oven at 60 ºC to dry the gel. The pressure was progressively decreased to 12 Pa, and the sample was left to dry overnight.

After drying, the organic xerogel monolith was retrieved and ground to a narrow particle size distribution. First, a coarse milling by hand using an agate mortar was performed; then, the organic gel particles were reduced to fine powder using a Fritsch planetary mill (Mono Mill P6). The sample was ground at 400 rpm for 24 cycles of 1 min each, followed by 15 s of rest. The powder was then pyrolyzed at 800 ºC under N_2 in a tubular oven using the following procedure in order to obtain the pristine CX. The temperature was increased (1) to 150 ºC at 1.7 ºC min^{-1} and held for 15 min; (2) from 150 to 400 ºC at 5 ºC min^{-1} and held for 60 min; and (3) from 400 to 800 ºC at 5 ºC min^{-1} and held for 120 min. Finally, the oven was let to cool down to room temperature overnight.

The initial sample obtained after pyrolysis is called LPH (low-pH carbon xerogel) hereafter.

2.2. Physical activation with CO_2

Physical activation of the pristine CX took place in the same tubular oven used for pyrolysis, switching from N_2 (Air Liquide N25) to CO_2 (Air Liquide N27). The oven was supplied with nitrogen and carbon dioxide by a three-way valve, so that it was possible to switch from one gas to the other. Once the pyrolysis process was completed, the oven temperature was increased from 800 ºC to 900 ºC and the atmosphere was then changed from N_2 to CO_2.The duration of the procedure was 5 h and the gas flow rate was chosen equal to 0.004 mol min^{-1}. Finally, the atmosphere was switched back to N_2 for cooling and the sample was removed from the oven.

The activated sample is called LPH-A hereafter.

2.3. Chemical Vapor Deposition

Chemical Vapor Deposition (CVD) was performed in a stainless-steel tubular oven, following the process described in a previous study [16] and involving ethylene cracking at moderate temperature. The oven was first heated at 685 ºC under inert atmosphere (N_2, flow rate: 0.025 mol min^{-1}). The quartz boat containing the CX powder was introduced into the oven once the target temperature had been reached, using a reverse flow system to maintain the protective inert atmosphere inside the oven. The reactive mixture was then introduced into the system (total flow rate: 0.082 mol min^{-1}), consisting of 80% ethylene (Air Liquide N25, 0.066 mol

min^{-1}) and 20% N_2 (Air Liquide Alphagaz 1, 0.016 mol min^{-1}). The duration of the CVD treatment was set at either 30 or 60 min, while the temperature was maintained at 685 °C. The atmosphere was then switched back to 100% N_2 (flow rate: 0.025 mol min^{-1}) for purging once the coating process was completed. Finally, after complete elimination of the ethylene, the oven temperature was increased to 900 ºC and held for 2 h. The oven was then cooled down under N_2 atmosphere, the resulting powders were collected and weighed again in order to observe the mass gain obtained by coating.

Three coated samples were produced: (i) non-activated LPH coated for 30 min (LPH-C30), (ii) activated LPH coated for 30 min (LPH-A-C30) and (iii) activated LPH coated for 60 min (LPH-A-C60). Table 1 summarizes the post-treatment conditions applied to the five carbons investigated in this research.

Table 1. Description of samples according to their surface modifications.

Sample	CO_2 activation	CVD coating
LPH	No	None
LPH-C30	No	30 min
LPH-A	Yes	None
LPH-A-C30	Yes	30 min
LPH-A-C60	Yes	60 min

2.4. Physicochemical characterization of carbon materials

The pore texture of the five CX powders was analyzed by N_2 adsorption-desorption measurements. Prior to the measurements, the samples were degassed under high vacuum (2×10^{-4} Pa) at room temperature for 5 h and at 270 °C for 2 h. Isotherms were acquired at -196 °C using a Micromeritics ASAP 2420 analyzer. The specific surface area, A_{BET}, was calculated using the Brunauer-Emmet-Teller (BET) [27] equation, in each case choosing the relative pressure range to fulfil Rouquerol's criterion [28]. The Dubinin-Radushkevich equation was used to calculate the micropore volume, V_{μ}.

Hydrogen adsorption-desorption measurements were also carried out to assess the materials microporosity in more detail. Samples were degassed under high vacuum at 180 °C for 24 h before isotherms were acquired at -196 °C using a Micromeritics 3Flex analyzer. The 2D non-local density functional theory for heterogeneous surface (2D-NLDFT-HS) was applied simultaneously to the N_2 and H_2 adsorption isotherms using Micromeritics' SAIEUS software

to obtain pore size distributions (PSDs). Textural properties such as specific surface area (S_{DFT}), total pore volume ($V_{T,DFT}$), and ultramicro-, supermicro- and mesopore volumes ($V_{u\mu,DFT}$, $V_{s\mu,DFT}$ and $V_{meso,DFT}$, respectively) were calculated from the PSDs obtained.

Mercury porosimetry was performed to obtain information on CX meso-macroporosity, as the N_2 adsorption technique is not suitable for analyzing the widest pores of the materials. Measurements were conducted with a Quantachrome Poremaster 60 in a pressure range from 0.01 to 400 MPa. The analysis was carried out for all samples in powder form. Analysis of the mercury intrusion data enabled determining the cumulated pore volume, V_{Hg}, and the PSD for pores with diameters greater than 3.8 nm. The PSD was calculated using the Washburn [29] equation, valid for mercury intrusion without sample crushing; the values considered for the equation parameters were (i) an average value for the liquid/solid contact angle of 140° and (ii) a mercury surface tension of 0.485 N m^{-1}.

Scanning electron microscopy (SEM) was used to observe the carbon morphology and determine the size of carbon nodules, D_n. Images were obtained using a Tescan CLARA FEG-SEM at 15 kV under high-vacuum conditions. The samples were gold-coated in a sputtering device (Balzers, SCD004 sputter coater, Vaduz, Liechtenstein) and mounted with carbon adhesive tape prior to observation. Average nodule sizes were calculated based on a minimum of 30 measurements per sample.

To observe the impact of activation, samples were observed by transmission electron microscopy (TEM) using a FEI Tecnai F20-S-TWIN microscope and a JEOL JEM-ARM 200F Cold FEG equipped with a spherical aberration probe corrector; both operations were run using an acceleration voltage of 200 kV. Samples were prepared by suspending the powder in ethanol. Then, one or two drops of the suspension were deposited on a copper grid with a holey carbon film. High-resolution imaging was performed by controlling the electron dose to avoid electron beam-induced artefacts. Fast Fourier Transform on HR-TEM images was used to obtain the d-spacing (d_{002}) between graphene layers.

X-ray diffraction was used to assess the crystallinity of the materials before and after CVD coating. Measurements were performed in Bragg-Brentano configuration for diffraction angles 2θ between 10° and 80° and a step size of 0.021° with a Bruker AXS D8 Advance diffractometer using a copper X-ray source ($\lambda_{K\alpha}$ = 0.15418 nm). A shallow sample holder with a zero-background single-crystal Si plate was used to minimize sample transparency. The XRD patterns were analyzed using the model developed by Mallet-Ladeira [30]. The average lateral

size of the graphene domains (L_a) and the average stacking thickness of the graphene layers (L_c) were determined using Scherrer's equation from reflections (10l) and (002), respectively.

Raman spectra were recorded between 200 and 3800 cm^{-1} using a Horiba XploraRa Raman spectrometer equipped with a 50× long-range objective. A circularly polarized laser (λ = 532 nm) filtered to 10% of its maximum energy and a holographic grating of 1200 lines mm^{-1} were used. For each material, 5 to 7 different zones (or grains) were studied, and the resulting spectra were averaged before analysis.

TG-DSC measurements were conducted with a Setaram Sensys Evo equipment. In order to evaluate thermal behavior, the samples were heated up to 800 °C at a heating rate of 3°C min^{-1} under an air flow of 20 mL min^{-1}.

Elemental analysis (EA) was performed in a Vario EL Cube analyzer (Elementar) to measure bulk C, H, N, S and O contents. Samples were dried overnight at 105 °C to remove moisture, and then a small amount of material (~2 mg) was placed in the equipment to be burned in a furnace from which the gases were separated using trapping and chromatographic columns prior to detection. A thermal conductivity detector quantified the gases, from which carbon, hydrogen and nitrogen contents could be calculated, sulfur being measured using a specific infrared detector. Oxygen content was measured separately in another column using a similar procedure.

2.5. Electrode manufacturing

Xanthan gum (Sigma-Aldrich) was used as a binder for the electrode manufacturing, as it preserves the pore texture (even the micropores) of the carbon material in the electrode configuration, meaning that the specific carbon surface areas measured on the powder and on the final electrode are expected to be the same [31]. This procedure also avoids the use of toxic solvents and fluorinated polymers as binders. Prior to spraying, the ink was prepared in MilliQ water with 12 wt.% solids, including CXs and xanthan gum (Sigma-Aldrich) as a binder, in a weight ratio of 92:8. The mixture was magnetically stirred at room temperature for 3 h. The prepared ink was sprayed onto pre-weighed stainless-steel discs (Type 304, 15.5×0.55 mm, MTI corp.), used as current collectors, *via* an airbrush (Harder & Steenbeck) and dried overnight at 60 °C. The obtained electrodes were then weighed and stored in a glovebox under Ar. The mass loading of active material ranged from 1.5 mg cm^{-2} to 2 mg cm^{-2} for all samples.

2.6. Electrochemical characterization

Cyclic voltammetry (CV) and galvanostatic charge-discharge methods were used to assess the electrochemical performance and further characterize the materials. In order to ensure the reproducibility, the tests were conducted at least on two different cells of identical composition and repeated up to 3, 4 or 5 times if more than 10% difference between the results was obtained.

CV was used to analyze the accessibility of the electrolyte to the surface of the electrode material. To this end, a supercapacitor-like setup with two CX electrodes was built in two-electrode coin-cell (CR2032) with glass fiber separator (Whatman, 1 mm-thick) under Argon atmosphere. Electrodes of similar masses were used so as the carbon surface was the same at both electrodes. CV experiments were conducted between cell voltages of -0.3 V and 0.3 V at 20 mV s^{-1} for all samples with commercial NP30 (1 mol L^{-1} solution of sodium hexafluorophosphate in a mixture of ethylene carbonate and dimethyl carbonate (EC/DMC, 1:1 mass ratio)) as electrolyte; *i.e.* the same electrolyte as the one used in the half-cells described below. However, for LPH-A, which displays a high surface area, the scan rate was later decreased to 0.1 mV s^{-1}. The specific capacitance (in F g^{-1}) of the cell was calculated as [32]:

$$C_{spec} = \frac{\int i(V)dv}{2\mu m \Delta V} \quad (1)$$

where the integral, which corresponds to the area of the CV curve, is the total charge (A.V), μ is the scan rate (V s^{-1}), m is the total mass of active material in two electrodes (g) and ΔV is the potential window of cycling (V). The calculated capacitance was divided by the total mass of active material (CX in both electrodes in this case) to obtain the specific cell capacitance.

Electrochemical characterizations in half-cell configuration were carried out by using a two-electrode coin-cell (CR2032) setup with CX as working electrode, sodium metal (Sigma-Aldrich) as counter- and reference electrode, a glass fiber separator (Whatman, 1 mm-thick), and commercial NP30 (1 mol L^{-1} solution of sodium hexafluorophosphate in a mixture of ethylene carbonate and dimethyl carbonate (EC/DMC, 1:1 mass ratio)) as electrolyte. The coin cells were assembled in a glovebox under Ar atmosphere (O_2 and H_2O concentrations < 1 ppm).

To evaluate the materials' performance at both low and high C-rates, the cells were cycled between 0.0 and 2.5 V *vs.* Na^+/Na for 5 cycles at C/20 (which corresponds to 18.6 mA g_{carbon}^{-1}, calculated considering the hypothetical formation of a NaC_6 phase during sodiation with a theoretical specific capacity of 372 mAh g^{-1}), C/10, C/5, C/2, C, 2C and 5C, and then for an additional series of 25 cycles at C/20. A rate of C/n thus corresponds to the insertion of one

Na^+ ion for every 6 carbon atoms, in n hours. ICE and capacity values were calculated from the first cycle of the above-mentioned C/20 C-rate cycling.

3. Results and discussion

The powders were characterized in terms of their physicochemical and electrochemical properties. The results obtained for the pristine carbon xerogel (LPH) and the coated carbon xerogel (LPH-C30) were reused from a previous study [16] as a basis for comparison with activated samples (without or with CVD coating).

3.1. Physicochemical properties of carbon xerogels

Sample mass changes were calculated by weighing the powders before and after the CVD and/or activation procedures. For the LPH sample, 4% increase in mass was observed after 30 min of CVD treatment. When LPH was treated under CO_2, the activated sample, LPH-A, displayed a mass loss of around 50%. The mass gain of LPH-A during CVD treatment is much higher than in the case of LPH: 9% for 30 min and 19% for 60 min of CVD treatment. However, SEM images (Figure SI.1) show no significant difference in nodule size, D_n, or any other feature of the material morphology, either after activation (Figure SI.1c) or after coating (Figures SI.1b, SI.1d and SI.1e) compared with the pristine CX sample LPH (Figure SI.1a).

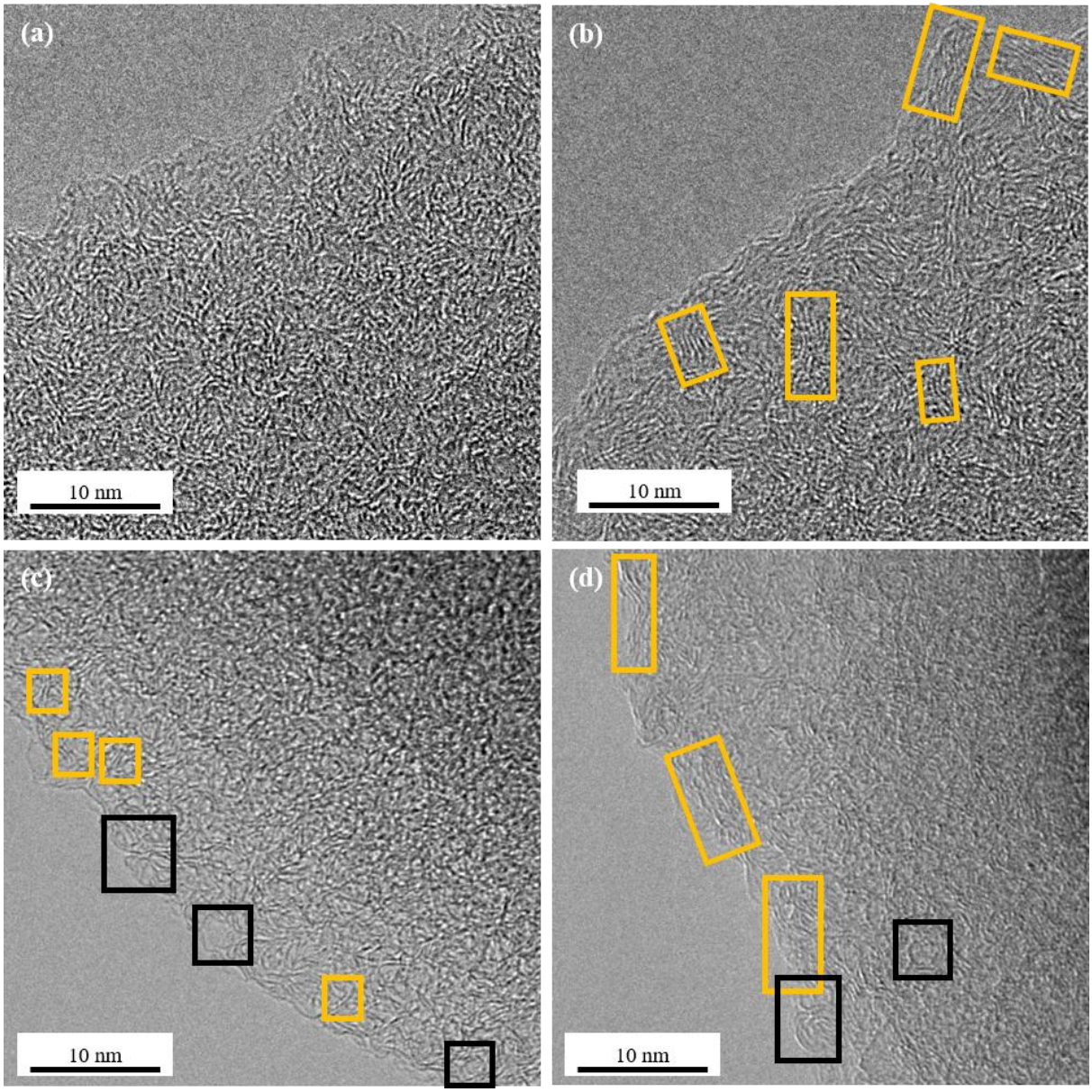

Figure 1. TEM images of samples (a) LPH, (b) LPH-C30, (c) LPH-A, (d) LPH-A-C60. In yellow: turbostratic domains. In black: onion-like structures.

All samples were observed by TEM to distinguish the organization of the carbon layers (Figure 1). As observed before [16], CVD coating seems to introduce a more ordered structure. Indeed, more organized carbon layers can be observed near the outer surface of the nodules. Especially, for the LPH-A-C60 sample, very extensive graphene-like sheets, about 10 nm long and a few nm thick, can be observed. The sheet stacks appear shorter and thinner in the case of sample LPH-C30. Meanwhile, the activated samples seem to feature onion-like structures. These onion-like structures and curvatures have already been observed in the literature [33-34].

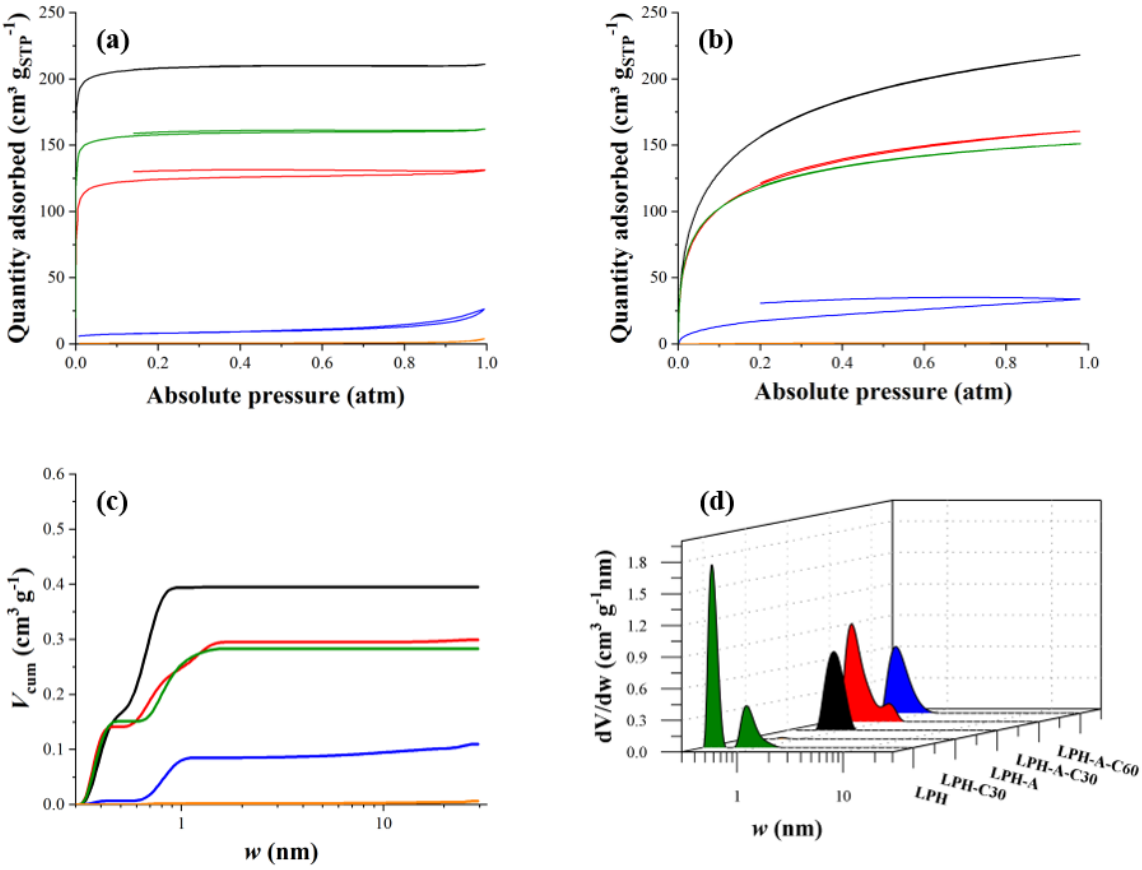

Figure 2. Pore texture analysis from gas sorption. (a) N_2 and (b) H_2 adsorption-desorption isotherms at -196 °C. (c) Cumulative pore volumes and (d) pore size distributions of samples LPH (—), LPH-C(—), LPH-A (—), LPH-A-C30 (—) and LPH-A-C60 (—).

N_2 and H_2 adsorption were used to understand the micro-mesoporous texture and to determine the specific surface area of the samples (Figure 2). The reference sample (LPH) is strictly microporous, with a BET area A_{BET} equal to 645 $m^2\ g^{-1}$ and a micropore volume V_μ of 0.25 $cm^3\ g^{-1}$ (Table 2). CO_2 activation does not modify the pore texture of the carbon xerogel in terms of pore type, as the LPH-A sample remains strictly microporous (type I isotherm). However, as expected, an increase in BET area is observed, up to 855 $m^2\ g^{-1}$. The micropore volume also increases, up to 0.32 $cm^3\ g^{-1}$. The CVD coating induces significant changes in the low-pressure region corresponding to the micropores, especially for the LPH-C30 sample. As observed in a previous study [16], the carbon coating produced by CVD blocks the micropores and reduces the total specific surface area. The A_{BET} value thus decreases to 2 $m^2\ g^{-1}$ after 30 min of CVD treatment on sample LPH. However, when the same duration of CVD treatment is applied to the LPH-A sample, A_{BET} only decreases from 855 to 505 $m^2\ g^{-1}$ (sample LPH-A-C30), while

V_μ is still equal to 0.20 $cm^3\ g^{-1}$. This shows that the micropores are not entirely covered by the carbon coating. Therefore, in the case of the activated sample, a longer CVD time is needed to mask completely the micropores. Indeed, 60 min of the coating process decreases the specific surface area and microporous volume down to 30 $m^2\ g^{-1}$ and 0.03 $cm^3\ g^{-1}$, respectively (sample LPH-A-C60). Given the higher mass uptake, it is possible that all the micropores are blocked, with the remaining surface corresponding to the roughness of the coating, even though no significant morphological difference can be seen on SEM images (Figure SI.1). The nodule size distribution of all samples remains identical, whatever the post-treatment (Figure SI.2), leading to an average nodule value D_n of 2.0 nm (Table 2). Another important difference for LPH-A-C60 is reflected in the shape of the N_2 adsorption isotherm, which features a small volume of meso/macropores (type I + type II isotherm). Since the two uncoated materials (LPH and LPH-A) show no mesoporosity at all, the newly introduced mesoporous structure could again come from the thicker coating of LPH-A-C60 (Figure 2a).

H_2 adsorption isotherms are shown in Figure 2b, while the cumulative pore volumes as a function of pore width, *w*, and the derived pore size distributions, calculated by combining the N_2 and H_2 adsorption isotherms, are presented in Figures 2c and 2d, respectively. The total specific surface area of the samples, S_{DFT}, and the pore volume in the mesopore, supermicropore and ultramicropore range ($V_{meso,DFT}$, $V_{s\mu,DFT}$ and $V_{u\mu,DFT}$, respectively) are displayed in Table 2. As with the N_2 adsorption isotherms, an increase in S_{DFT} can be observed after CO_2 activation, from 1115 $m^2\ g^{-1}$ for sample LPH to 1535 $m^2\ g^{-1}$ for sample LPH-A. This change corresponds mainly to an increase in the ultramicropore volume (pore sizes < 0.7 nm). As expected, CVD treatment proves to be an effective way to mask/fill micropores. Indeed, the S_{DFT} value of LPH-C30 decreases to 70 $m^2\ g^{-1}$. LPH-A-C30 and LPH-A-C60 have S_{DFT} values equal to 1150 $m^2\ g^{-1}$ and 240 $m^2\ g^{-1}$, respectively. Finally, an increase in $V_{meso,DFT}$ can be observed for LPH-A-C30 and LPH-A-C60, which confirms the observations on the N_2 isotherms. Note some several isotherms related to LPH-A-C30 and LPH-A-C60 in figures 2a and 2b present a small hysteresis at low pressure. This phenomenon, which is quite reproducible from one measurement to another, might be due to the partial coverage of the micropores by the CVD layer, which would desorption more difficult. In the case of N_2 adsorption, this phenomenon could also be related to the presence of supermicropores [35]. In any case, data issued from N_2 and H_2 adsorption-desorption measurements presented in Table 2 were calculated using the adsorption branch of the isotherm.

Table 2. Morphological parameters and pore texture data for all samples.

Morphological parameters			**Textural parameters**						
			Determined by N_2 adsorption at -196 °C		Determined by combination of N_2 and H_2 adsorption at -196 °C				
Sample	D_n[a] (µm)	d_p[b] (µm)	A_{BET}[c] ($m^2\ g^{-1}$)	V_μ[c] ($cm^3\ g^{-1}$)	S_{DFT}[d] ($m^2\ g^{-1}$)	$V_{u\mu,DFT}$[d] ($cm^3\ g^{-1}$)	$V_{s\mu,DFT}$[d] ($cm^3\ g^{-1}$)	$V_{meso,DFT}$[d] ($cm^3\ g^{-1}$)	$V_{T,DFT}$[d] ($cm^3\ g^{-1}$)
LPH	2.0	3.9	645	0.25	1115	0.16	0.12	0.00	0.28
LPH-C30	2.0	3.9	2	<0.01	70	0.00	0.02	0.00	0.05
LPH-A	2.0	3.9	855	0.32	1535	0.31	0.09	0.00	0.40
LPH-A-C30	2.0	3.9	505	0.20	1150	0.19	0.10	0.004	0.30
LPH-A-C60	2.0	3.9	30	0.03	240	0.02	0.07	0.024	0.11

[a] D_n: average nodule size calculated from SEM images.

[b] d_p: pore diameters determined by Hg porosimetry.

[c] A_{BET}: BET area and V_μ: micropore volume, calculated from nitrogen adsorption-desorption isotherms at -196 °C.

[d] S_{DFT}, $V_{u\mu,DFT}$, $V_{s\mu,DFT}$, and $V_{T,DFT}$: specific surface area, ultramicropore, supermicropore, and total pore volume calculated from the PSD obtained from nitrogen and hydrogen adsorption isotherms at -196 °C.

Hg porosimetry curves for powder samples are shown in Figure 3, and presented as cumulative pore volume *vs.* pressure. Average pore sizes were calculated using Washburn's law from the intrusion step visible between 2 and 5 µm, the volume change occurring at lower pressure being attributed to powder compaction. Average pore diameters (d_p) were calculated to be equal to 3.9 µm for all samples (Table 2). These pores correspond to the voids between the carbon nodules observed in Figure SI.1, and no significant change is noticed after activation and/or CVD coating.

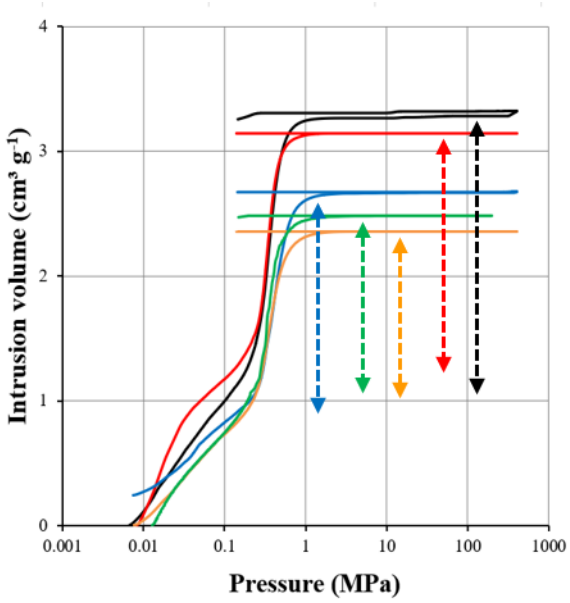

Figure 3. Mercury porosimetry curves for samples LPH (—), LPH-C30 (—), LPH-A (—), LPH-A-C30 (—) and LPH-A-C60 (—). Vertical arrows represent the mercury intrusion step. The increase in volume at lower pressure is due to powder compaction.

The XRD patterns of the samples are shown in Figure 4. The curves have been shifted upwards for better legibility. Overall, all samples display the same bands at the same diffraction angles. Namely, a first broad band at around 2θ = 23° (002) and a second broad band at around 2θ = 43° (10l) is observed; both are quite common for highly disordered carbons. A peak at around 2θ = 26° can be observed for samples LPH-C30 and LPH-A-C60. This peak, which is not always observed for CVD-coated samples, is in fact ascribed to carbon deposits formed outside the carbon xerogel during the CVD procedure (*e.g.* formed on the quartz boat or oven walls); it is considered as an impurity. Furthermore, the intensity of the (002) band is higher for all CVD-coated samples, probably due to the contribution of the coating. However, CO_2 activation leads to the opposite effect, as the intensity of the (002) band is much lower for the LPH-A

sample than for the pristine LPH. The complete list of structural parameters values is shown in Table 3. The coherence length, L_a, increases after CO_2 activation, from 3.38 nm (LPH) to 3.71 nm (LPH-A). Upon CVD treatment, L_a increases after 30 min (LPH-C30: 3.82 nm; LPH-A-C30: 4.22 nm), and remains unchanged when the CVD time is prolonged to 60 min (LPH-A-C60: 4.22 nm). Regarding L_c, there is an increase for sample LPH-A compared to sample LPH, indicating that CO_2 activation might increase the average stacking thickness of the graphene layers. This might be due to the preferential elimination of carbon defects upon CO_2 activation, due to a higher reactivity of those atoms during the treatment. On the contrary, L_c decreases for the coated samples. Finally, a very slight decrease in the graphene interlayer distance, $d_{(002)}$, can be observed for carbon-coated samples compared with their uncoated counterparts. Overall, the XRD and TEM observations do not indicate any significant structural change.

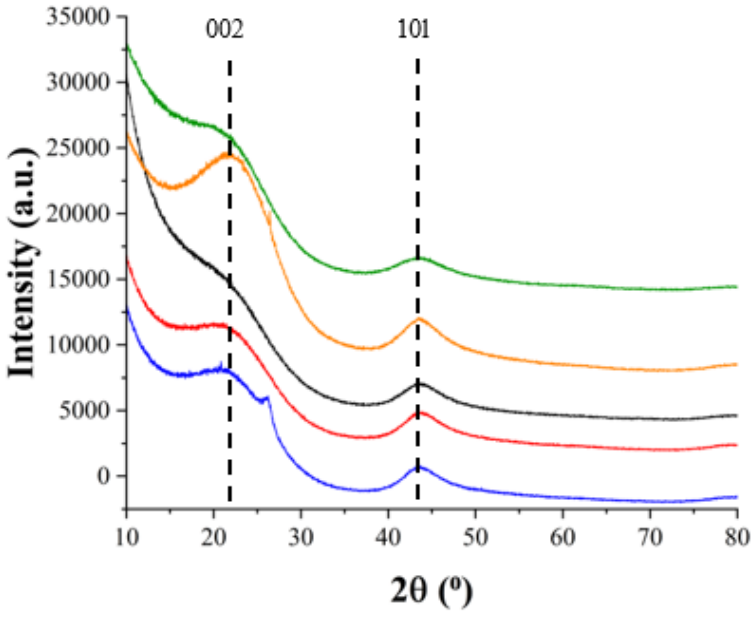

Figure 4. X-ray diffraction patterns of samples LPH (—), LPH-C30 (—), LPH-A (—), LPH-A-C30 (—) and LPH-A-C60 (—).

Table 3. Structural parameters of the samples.

			LPH	LPH-C30	LPH-A	LPH-A-C30	LPH-A-C60
XRD	d_{002}	(nm)	0.405 ± 0.001	0.392 ± 0.001	0.400 ± 0.001	0.398 ± 0.001	0.401 ± 0.001
	L_c	(nm)	1.12 ± 0.19	1.02 ± 0.11	1.32 ± 0.16	1.10 ± 0.09	1.15 ± 0.05
	L_a	(nm)	3.21 ± 0.01	3.85± 0.001	3.71 ± 0.06	4.22 ± 0.03	4.22 ± 0.02
TEM	d_{002}	(nm)	0.409 ± 0.040	0.392 ± 0.037	0.407 ± 0.090	0.402 ± 0.070	0.397 ± 0.070

TG-DSC was used to distinguish the carbon xerogel from the carbon coating deposited by CVD, especially on the activated and activated + coated samples. The results of TG-DSC measurements (Figure SI.3) are very similar for all of the investigated samples, with a first small mass loss between 20 and 150°C that can be ascribed to the evaporation of water adsorbed on the surface of the material and a very important mass loss between 300 and 650°C corresponding to the combustion of the carbon. The onset of the major mass loss is slightly shifted towards a higher temperature for the CVD-coated samples and this shift is more important with CVD duration. Accordingly, the corresponding heat flow curves show this same shift. These observations suggest a slightly increased thermal stability of the coated carbons.

The detailed analysis of Raman spectra can be found in S.I. (Figures SI.4 and SI.5). It shows that, while LPH and LPH-A samples are indeed disordered carbons, the CVD treatment produces a material with a more ordered nanotexture, especially sample LPH-A-C60 given the longest deposition time, and thus mass uptake. This again is coherent with other observations indicating that the carbon layer deposited by CVD is (at least partially) graphitized.

Elemental analysis (Table 4) shows a significant difference in terms of oxygen content. The low oxygen content (2.4 wt.%) of LPH increases by 50% upon CO_2 activation, as LPH-A contains 3.6 wt.% oxygen. This increase is probably due to (i) the CO_2 activation reaction itself and (ii) the oxidation of the carbon when the sample is removed from the oven. Indeed, activation starts with the dissociative chemisorption of CO_2 on the carbon surface to form a surface oxide and carbon monoxide [36]. The surface oxide is subsequently desorbed from the surface, further developing the micropores. Finally, the remaining end-plate carbon atoms, which are more numerous after CO_2 treatment, oxidize on contact with air. However, although CVD coating slightly increases the oxygen content of LPH sample, from 2.4 to 2.8 wt.% for LPH-C30, it reduces the oxygen content of the LPH-A sample down to 3.2 wt.% and 2.3 wt.%

after 30 min and 60 min of CVD treatment, respectively. Meanwhile, a general trend can be observed regarding hydrogen content: overall, the CVD-coated samples contain less hydrogen and more carbon than their uncoated counterparts do. This trend agrees well with TEM observations of longer graphitic-like domains after CVD coating. Finally, it seems that the CVD treatment induces a slight increase of the nitrogen content, possibly coming from the fact that the atmosphere used is an ethylene-nitrogen mix.

Table 4. Elemental analysis of carbon xerogels before and after CO_2 activation and CVD treatment.

Sample	**N** (wt.%)	**C** (wt.%)	**H** (wt.%)	**S** (wt.%)	**O** (wt.%)
LPH	0.1	96.2	0.9	0.0	2.4
LPH-C30	0.2	98.0	0.3	0.0	2.8
LPH-A	0.1	93.6	0.6	0.0	3.6
LPH-A-C30	0.1	95.2	0.5	0.0	3.2
LPH-A-C60	0.4	97.2	0.4	0.0	2.3

3.2. Electrochemical performance of carbon xerogels

Following morphological and structural characterization, the electrochemical performance of the samples as negative electrode materials for Na-ion battery was assessed in a half-cell setup. The data are gathered in Table 5. $C_{tot,disch}$ represents the total capacity at first discharge (*i.e.* first sodiation) while C_{rev} is the capacity delivered by the first charge (*i.e.* first desodiation). The irreversible capacity, C_{irrev}, is calculated as the difference between $C_{tot,disch}$ and C_{rev}. Meanwhile, the Initial Coulombic Efficiency, ICE, is calculated as the ratio between C_{rev} and $C_{tot,disch}$. Finally, the capacities in both the slope region (above 0.1 V *vs.* Na^+/Na) and the low-voltage plateau (below 0.1 V) of the first discharge curve (*i.e.* first sodiation) are reported as C_{slope} and $C_{plateau}$, respectively. Note that, in some cases, two distinct slope regions were detected. C_{slope} has thus been divided into C_{slope1} and C_{slope2} in Table 5. The curves corresponding to the first cycle are shown in Figure 5. Additionally, cyclic voltammetry was performed in a symmetrical supercapacitor setup in order to understand the accessibility of the electrolyte to the surface of the electrode material; in this context, the specific capacitance, C_{spec} is calculated using Equation 1. Cyclic voltammograms are shown in Figure 6. Finally, the

retention capacity of the electrodes after various C-rate cycling is reported as C_{ret}; this parameter compares the first 5 cycles at C/20, at the start of cycling, and the last 5 cycles at C/20 after the various C-rate cycling sequence, in order to measure the stability of the electrodes. Figure 7 provides a schematic representation of the evolution of the carbon nodule structure with post-treatments, along with its assumed interaction with the electrolyte, as discussed in the next paragraphs. Finally, the overall results (capacity and faradaic yield *vs.* cycle number and C-rate) are shown in Figure 8.

The total discharge capacities, $C_{tot,disch}$, are close to each other for all samples: values are around 300-357 mAh g^{-1} (Table 5, Figure 5). However, the reversible capacities at first cycle, C_{rev}, and therefore the ICEs, are strikingly different. The LPH sample has a C_{rev} equal to 248 mAh g^{-1}, which corresponds to an ICE of 80%. After 30 min of CVD treatment, the reversible capacity of LPH-C30 is measured as 298 mAh g^{-1} (84% ICE). As indicated previously [16], the difference in reversible capacity (248 *vs.* 298 mAh g^{-1}) is probably due to micropore closure by CVD and thus to a larger volume of closed micropores in LPH-C30. Since N_2 adsorption shows a huge difference in A_{BET} between these two samples (645 *vs.* 2 m^2 g^{-1} for LPH and LPH-C30, respectively), a huge modification in ICE would have been expected as well, which is not the case; this indicates that A_{BET} is not directly related to ICE values. It must be pointed out that our previous study also showed that nodules of different sizes could achieve different ICEs (29% for a 50 nm nodule size *vs.* 80% for a 2 µm nodule size), even though these CX carbons have very similar specific surface areas, as measured by N_2 adsorption (A_{BET} ~600 m^2 g^{-1}), with a majority of micropores. Therefore, it was proven that the ICE cannot be directly correlated with A_{BET}.

The hypothesis behind this peculiar result was that the electrolyte does not always access the micropores, although the latter are open and available to N_2 or H_2 gases; this hypothesis will be discussed below. In contrast to samples LPH and LPH-C30, the LPH-A sample shows a very low reversible capacity, 62 mAh g^{-1}, which corresponds to 18% ICE. This is not surprising at first sight, given the increase in surface area. However, upon activation, A_{BET} increased by only 30% (from 645 to 855 m^2 g^{-1}), and S_{DFT} by 38% (from 1115 to 1535 m^2 g^{-1}); this again shows that specific surface area measured by gas adsorption is not a good indicator of the ICE obtained in a half-cell. This calls for the determination of the surface to be considered for the development of the Solid Electrolyte Interphase (SEI). Most probably, CO_2 activation not only develops micropores (essentially ultra-micropores, see Table 2), but also makes some of them

more accessible to the electrolyte, by either enlarging the openings or modifying the properties of the carbon surface.

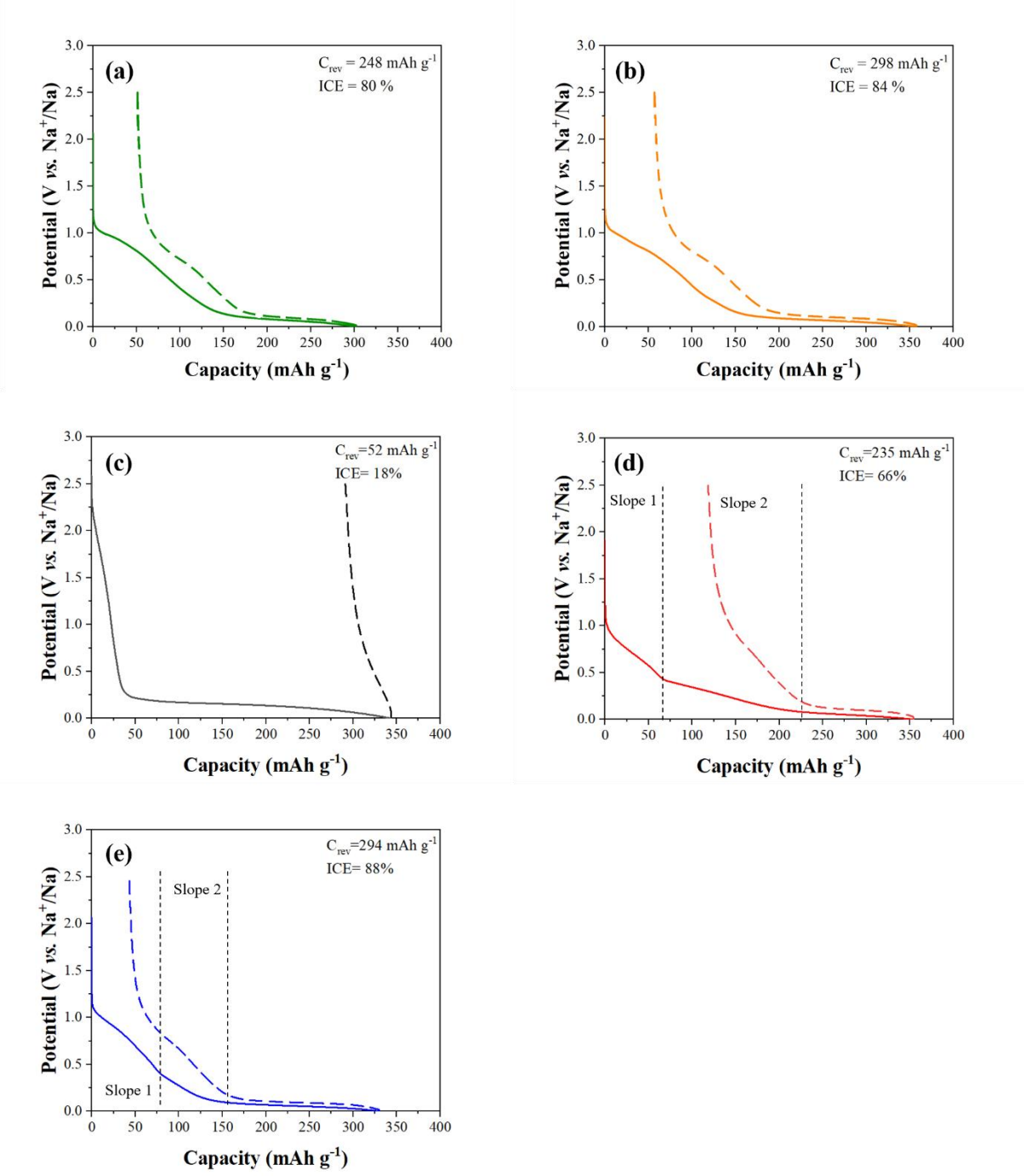

Figure 5. Galvanostatic charge (▬)-discharge (▪▪) profiles of samples: (a) LPH (▬), (b) LPH-C30 (▬), (c) LPH-A (▬), (d) LPH-A-C30 (▬), (e) LPH-A-C60 (▬). Half-cells with NP30 electrolyte, cycling at C/20 (corresponding to 18.6 mA g_{carbon}^{-1}).

Finally, as in the case of the LPH sample, the impact of the secondary carbon layer on the reversible capacity and ICE of the activated sample is striking. Indeed, the LPH-A-C30 sample

displays 66% ICE, which represents a good improvement over the LPH-A sample (18%). However, as the adsorption data show, the LPH-A-C30 sample still has a large surface area that remains uncovered by the CVD-deposited carbon layer, as A_{BET} remains high (505 m^2 g^{-1}). The relatively low ICE value indicated that access to the carbon surface is easier than for the pristine CX, LPH. Finally, a longer CVD treatment duration (60 min) leads to a further decrease in specific surface area (LPH-C-60: A_{BET} = 30 m^2 g^{-1}; S_{DFT} = 240 m^2 g^{-1}). It is clear that covering the micropores helps to improve the ICE and leads to very high reversible capacities, given that LPH-A-C60 reaches a C_{rev} of 294 mAh g^{-1} with 88% ICE, the highest values for all samples, although very close to those observed for LPH-C30 (C_{rev} of 298 m^2 g^{-1} and ICE equal to 84%). Those results are in line with observations upon cyclic voltammetry (CV). Figure SI.6 shows the first and fifth cycles performed in the same half-cell setup, at 0.1 mV s^{-1} scan rate. On first cycle, LPH and totally covered samples (LPH-C30 and LPH-A-C60) display expected cycle shapes, with reduction (sodiation) peaks associated to SEI formation and pore filling. The intensity and location of those peaks depend on the CVD deposition time. One observes large behavior differences for activated and partially covered samples (LPH-A and LPH-C30), probably because the SEI forms on both outer and inner nodule surface. Upon oxidation (desodiation), the intensity of the peak associated to sodium release is higher when the insertion plateau observed in Figure 5 is longer, no peak being visible for sample LPH. At cycle 5, all samples but LPH display classical behavior (adsorption + pore filling mechanisms).

As a general observation, the development of open micropores by CO_2 activation obviously deteriorates the electrochemical properties of CXs, even though the changes in ICE and C_{rev} cannot be directly related to the increase in specific surface area. However, covering the micropores of either the pristine or the activated sample with a secondary carbon layer by CVD is beneficial for both ICE and C_{rev}. It should also be noted that the C_{rev} and ICE values obtained are quite remarkable for samples heat-treated below 1000 °C. Indeed, hard carbons are generally processed at 1200-1800 °C, and their ICE and capacity usually increase when processed at higher temperatures [37]. In addition, oxygen content and other heteroatoms are known to affect the ICE of the electrodes. In this respect, a lower oxygen content can be seen for samples LPH-A-C60, LPH and LPH-C30 than for the others. These three samples also show a very high ICE compared to LPH-A and LPH-A-C30, which could indicate that the CO_2 activation process leads to the formation of O-rich surface, the latter being responsible for the irreversible reaction with sodium. Given the higher degree of graphitization and the reduced oxygen content observed in our study for coated samples, it is reasonable to infer that the CVD

layer has improved electronic conductivity compared to the pristine carbon. This more ordered carbon structure likely facilitates better electron transport at the interface.

To understand better the discrepancy between surfaces measured by gas sorption and ICE, the electrolyte accessibility to the electrode surface was studied by cyclic voltammetry (CV) using a symmetrical supercapacitor-like setup (Figure 6). Note that absolute capacitance values are highly dependent on the set-up and conditions, including the nature of the electrolyte. Here, the purpose of the CV experiments was to compare the samples with each other in a configuration that remains close to that of a half-cell, meaning that the capacitance values are not comparable with those found in the literature for carbon xerogels-based supercapacitors [38]. Note that, in principle, pseudocapacitance and quantum capacitance can impact capacitance of a supercapacitor. Here, the potential range was selected carefully to avoid pseudocapacitance given that hard carbons show capacitive behavior up to 3.4 V in $NaPF_6$ electrolyte [39]. Regarding quantum capacitance, it is known to be more pronounced for materials such as graphene and low dimension materials with very high specific surface area (from > 1000 m^2/g) [40]. Therefore, quantum capacitance is neglected and the measured capacitance is considered to be dominated by double layer capacitance.

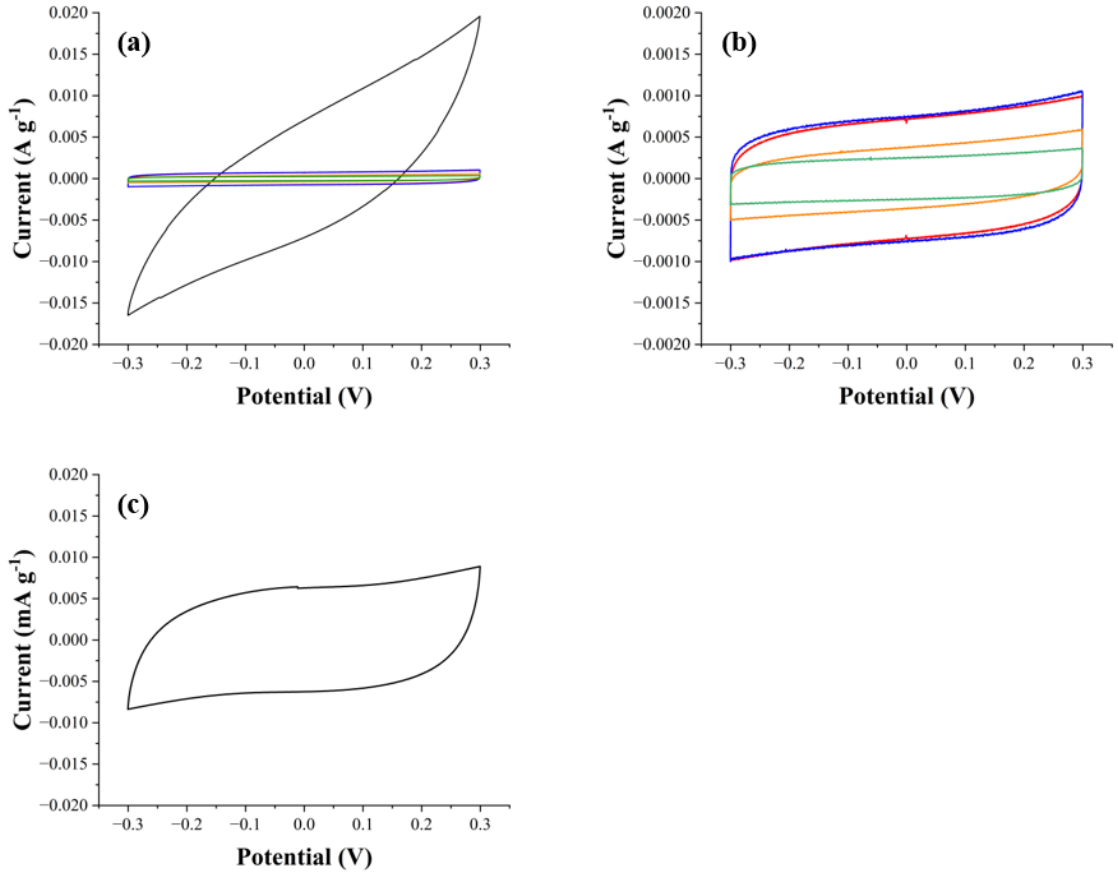

Figure 6. Cyclic voltammograms in a supercapacitor setup. (a) LPH (—), LPH-C30 (—), LPH-A (—), LPH-A-C30 (—), LPH-A-C60 (—) at 20 mV s^{-1}. (b) Close-up of samples without LPH-A-C60 at 20 mV s^{-1} scan rate. (c) LPH-A-C60 at 0.1 mV s^{-1} scan rate.

The LPH sample has a specific capacitance of 0.012 F g^{-1} *vs*. 0.017 F g^{-1} for LPH-C30 (Table 5); those values are very close. The capacitance should be directly proportional to the electrolyte/carbon interface area. Given the huge difference between the measured BET surface areas (655 and 2 m^2 g^{-1} for LPH and LPH-C30, respectively), it is obvious that the electrolyte/carbon area does not correspond to A_{BET}. In the case of the LPH-C30 sample, there is little ambiguity: since the micropores are not even accessible to N_2, the surface that can be in contact with the liquid electrolyte corresponds only to the nodule's external surface, $S_{n,ext}$, which has been geometrically calculated as equal to 2 m^2 g^{-1} [16] for the pristine CX and does not change with the CVD or CO_2 post-treatments. In the case of the LPH sample, and given the capacitance value similar to that of LPH-C30, the electrode/electrolyte interface area should be of the same order of magnitude. This clearly indicates that the electrolyte does not enter the micropores of the LPH sample, and that the electrode/electrolyte interface probably also corresponds to the external surface of the carbon nodules (Figure 7a and 7).

For the LPH-A sample, a significant increase in specific capacitance is observed, up to 0.27 F g^{-1}. This can be explained by the increase in micropore volume and surface area with CO_2 activation as well as increased oxygen amount in LPH-A since oxygenated-groups favor the access of the electrolyte to the structure [41]. Their impact is difficult to quantify at this stage. However, the increase in capacitance between LPH-C30 and LPH-A (~ 15-fold) is not proportional to the increase in specific surface area (multiplied by 426). As in the case of sample LPH, it is quite clear that not all the micropores of sample LPH-A are filled by the electrolyte, even though the available surface area is much larger than that of sample LPH (Figure 7c). After CVD coating, the specific capacitances of the activated samples drop to 0.035 F g^{-1} for LPH-A-C30 and 0.036 F g^{-1} for LPH-A-C60. Interestingly, the contact area between the electrolyte and the electrode material appears to increase slightly from LPH to LPH-C30 and from LPH-A-C30 to LPH-A-C60 (Figure 7d and e). In parallel, some mesoporosity was detected in the case of LPH-A-C60. This could mean that the structure of the carbon coating presents a certain roughness that would increase the electrolyte/electrode interface.

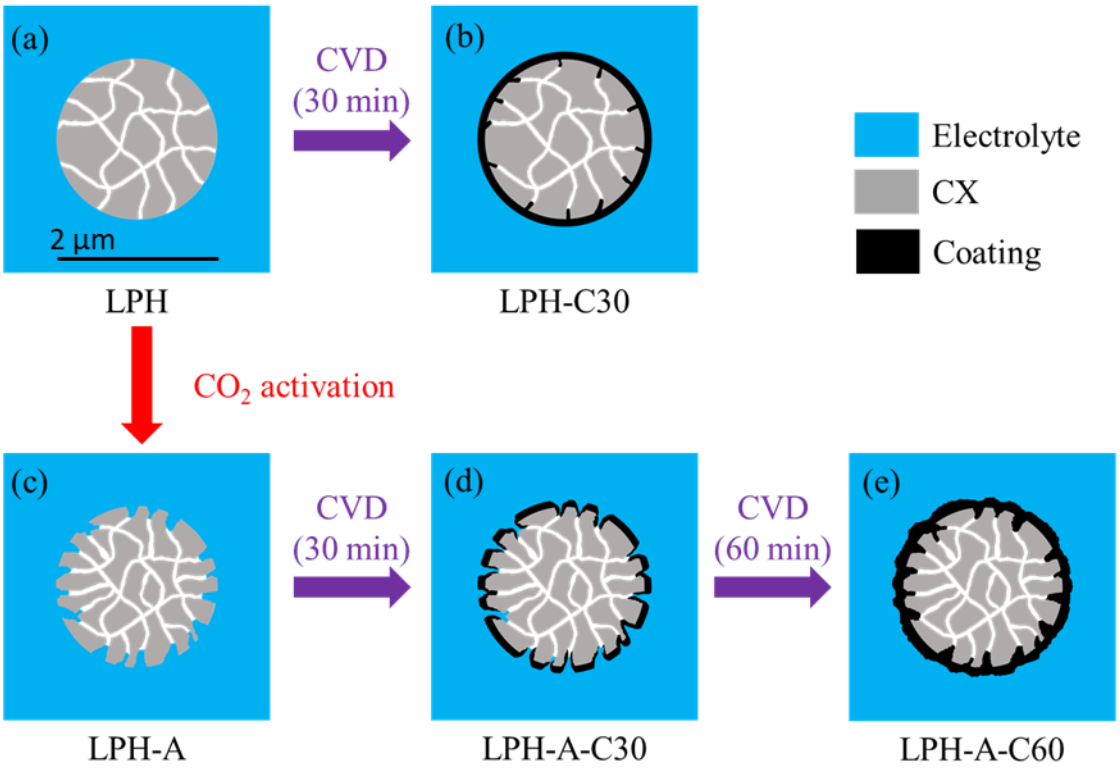

Figure 7. Schematic representation of the evolution of the carbon nodule structure and carbon-electrolyte contacts with post-treatments.

However, an increase in the electrolyte/carbon contact area should lead to a decrease in ICE, due to the formation of a SEI, which is not the case here. On the contrary, the ICE increases slightly with coating (from 80 to 84% for LPH and LPH-C30, and from 66 to 88% from LPH-A-C30 to LPH-A-C60). The SEI layer formation is in fact highly dependent on the reactivity of the electrolyte on the electrode material. The literature mentions that more ordered carbon structures show improved ICE performance as Na-ion battery anodes [10], pointing to a lower reactivity of ordered carbon surfaces with regard to SEI formation. Therefore, the surface of the CVD carbon layer is probably less reactive than that of the (activated) CX.

Coming back to the galvanostatic profiles (Figure 5), some differences can also be observed in the shape of the curves for the different samples. Firstly, the LPH and LPH-C30 profiles are very similar, as they both show a slope region and a plateau region (Figures 5a and 5b). However, an increase in the length of the plateau region can be detected after CVD treatment, reflecting the impact of micropore closure. The activated sample, LPH-A, displays a very different profile (Figure 5c) with almost no plateau but a very long slope region for the first sodiation. As discussed above, the capacity of LPH-A is highly irreversible due to its very large surface area, partially accessible to the electrolyte. As observed previously on the non-activated xerogel, the effect of coating is again visible on the galvanostatic profiles, as LPH-A-C30 and LPH-A-C60 both show a plateau and two clearly distinct slope regions at around 0.8 V and 0.3 V *vs.* Na^+/Na (Figures 5d and 5e), which are referred to as "slope region 1" and "slope region 2" hereafter. Although the dominant storage mechanisms on these regions are still debated, LPH-A-C30 shows a longer "slope 2" region than LPH-A-C60 (140 mAh g^{-1} *vs.* 77 mAh g^{-1}), while the "slope 1" region is similar for both samples (68 mAh g^{-1} *vs.* 66 mAh g^{-1}). However, this 2-slope profile disappears after the first sodiation: the change in slope is barely visible during the first desodiation, and totally disappears during the second sodiation (Figure SI.7). It is therefore highly likely that the presence of two distinct slope regions in the first cycle is related to the formation of the SEI layer. At the same time, the LPH-A-C60 sample shows a very high plateau capacity (159 mAh g^{-1}). This capacity is considerably higher than that of samples LPH (99 mAh g^{-1}), LPH-C30 (129 mAh g^{-1}) and LPH-A-C30 (108 mAh g^{-1}).

In relation to their full reversible capacities, plateau capacities correspond to 39%, 43%, 36% and 54% for electrodes LPH, LPH-C30, LPH-A-C30 and LPH-A-C60, respectively (Table 5). LPH-A-C30 has the lowest plateau ratio (36%), probably because the micropores are not

masked completely yet. These results indeed show that the formation of new micropores by CO_2 activation and their closure by a carbon layer *via* CVD increase the volume of closed micropores and lead to better electrochemical performance of the CXs.

Finally, the electrodes were cycled at different C-rates in order to understand the effect of activation and coating thickness on the rate capability (Figure 8). Firstly, the coulombic efficiency quickly stabilizes at around 100% for all samples except LPH-A and LPH-C30, both after the first cycles and after any change in C-rate during various C-rate cycling. The electrodes show similar behavior at low C-rates such as C/20, C/10 and C/5, as well as a dramatic drop in capacity after C/2. Although the LPH-C30 sample shows higher capacity than LPH at low cycling rate, it becomes equal around C/2 and lower from 1C and above. Furthermore, the plateau region disappears at higher C-rates, which can be interpreted as Na^+ ions not having enough time to fill the inner pores of the carbon nodules (Figure SI.8). Like the other samples, LPH-A can retain some capacity up to C/2, but values drop to 0 at higher C-rates. However, the coating improves the performance of the activated sample, as the capacity remains relatively high for both LPH-A-C30 and LPH-A-C60.

The capacities obtained for LPH-A-C60 at each C-rate are quite similar to those of the LPH sample, indicating a recovery from activation and an improvement over LPH-C30. The CVD layer may introduce a barrier to Na^+ diffusion due to its more compact morphology, which could explain the lower rate performance of LPH-C30 compared to LPH. However, increasing the contact area between electrode and electrolyte is known to be beneficial to rate capability, since it can provide a larger area for charge transfer [42-43]. Thus, the larger electrode-electrolyte interface area of LPH-A-C60 compared to LPH-C30 might be the reason for the better rate capability of the former carbon. Additionally, although it remains speculative, the onion-like structures observed in the activated sample have been reported to increase the rate capability, as they would be able to reduce Na^+ diffusion pathways [44]. Moreover, it has been also reported that curvatures introduced into hard carbons can benefit their performance by improving the adsorption of Na^+ ions [13]. The exact impact of these structures, however, needs to be studied further.

After cycling at various C-rates, the procedure was prolonged by 15 additional cycles at C/20 to determine the stability of the electrodes. Most samples recovered 91% to 95% of their initial capacity; LPH-A reached almost 100%, but its initial capacity was already very low (62 mAh g^{-1}). Interestingly, LPH-A-C60 also retained 95% of its initial capacity after 15 cycles at C/20,

while it decreased to 88% for LPH, 65% for LPH-C30 and 89% for LPH-A-C30. The capacity retention after the additional 15 cycles remained close to 100% for LPH-A, but, as mentioned previously, with a low initial capacity. The CVD-coated CX prepared without activation shows both high ICE and capacity, but low rate capability and stability. In contrast, LPH-A-C60 shows both high ICE and capacity without losing rate capability and stability. The development of micropore volume and the introduction of onion-like structures might be essential for charge transfer. Combining this with a carbon coating to limit contact between the carbon and the liquid electrolyte seems a good way to improve the electrochemical performance of hard carbons in NIB negative electrodes.

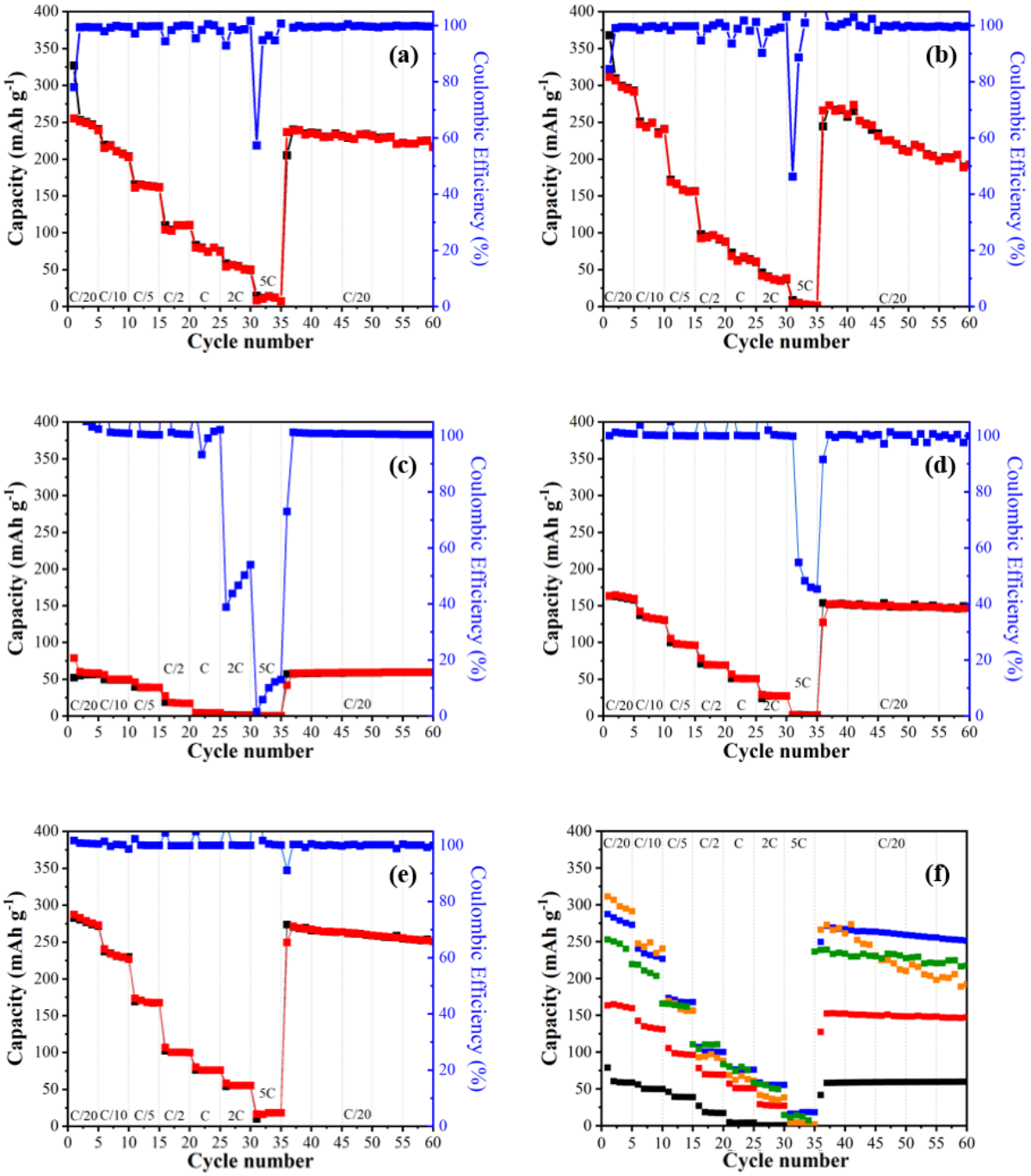

Figure 8. Galvanostatic charge-discharge performance at various cycling rates. (■) Desodiation capacity, (■) sodiation capacity and (■) coulombic efficiency for samples (a) LPH, (b) LPH-C30, (c) LPH-A, (d) LPH-A-C30, (e) LPH-A-C60. Figure (f) compares desodiation capacities of all samples: LPH (—), LPH-C30 (—), LPH-A (—), LPH-A-C30 (—), LPH-A-C60 (—).

Table 5. Electrochemical performance of the samples.

Sample	$C_{tot,disch}$[a]	C_{rev}[b]	C_{slope1}[a]	C_{slope2}[a]	$C_{plateau}$[b]	$C_{plateau}/C_{rev}$[b]	ICE	C_{ret}	C_{spec}
	(mAh g^{-1})	(mAh g^{-1})	(mAh g^{-1})	(mAh g^{-1})	(mAh g^{-1})	(%)	%	(%)	(F g^{-1})
LPH	300 (±3)	248 (±12)	170	-[c]	99	39	80 (±1)	88	0.012
LPH-C30	357(±17)	298 (±11)	184	-[c]	129	43	84 (±1)	65	0.017
LPH-A	343 (±18)	62 (±4)	62	-[c]	-[d]	-[d]	18 (±0.3)	100	0.270
LPH-A-C30	354 (±10)	235 (±6)	68	140	108	36	66 (±0.6)	89	0.035
LPH-A-C60	329 (±7)	294 (±5)	66	77	159	54	88 (±0.7)	95	0.036

[a] Calculated from the first discharge (*i.e.* first sodiation).
[b] Calculated from the first charge (*i.e.* first desodiation).
[c] Second slope region not observed.
[d] No plateau observed.

4. Conclusions

This study demonstrates the considerable impact of CO_2 activation and CVD carbon coating on carbon xerogels (CX) as negative electrodes in Na-ion batteries (NIBs). Targeting optimal surface characteristics, we synthesized a CX with ~2 µm nodules and an initial surface area of 645 $m^2\ g^{-1}$. Through CO_2 activation, microporosity was enhanced, while CVD coating effectively masked these micropores.

Direct CVD coating on the pristine CX achieved a very low specific surface area (A_{BET} = 2 $m^2\ g^{-1}$), resulting in high Initial Coulombic Efficiency (ICE = 84%) and substantial reversible capacity (C_{rev} = 298 mAh g^{-1}). By contrast, CO_2 activation alone increased the surface area, A_{BET} = 855 $m^2\ g^{-1}$, but significantly lowered the performance (ICE = 16%, C_{rev} = 62 mAh g^{-1}). Notably, subsequent CVD coating on the activated CX restored high performance, with an ICE of 88%, a reversible capacity of 294 mAh g^{-1}, and improved rate capability. Furthermore, capacitance studies indicated that specific surface areas measured by gas adsorption are not directly linked to the effective electrode/electrolyte interface where Solid Electrolyte Interphase formation occurs, emphasizing that micropore accessibility to the electrolyte must be limited to improve performance. Additionally, although the capacitance can be linked to SEI formation for the materials that has the same surface structures, it is not directly indicative for carbon xerogels that are coated with a more ordered structure.

These findings suggest that the combination of microporosity and selective surface masking can produce low-temperature carbon materials with excellent properties for NIB applications.

With their highly tunable structure, CXs are promising candidates for further *in situ* studies on Na^+ storage mechanisms, providing a foundation for the rational development of high-performance NIB electrodes. Additionally, this works further shows that CO_2 activation and CVD carbon deposition techniques enable the manufacturing of materials with both low surface area (which limits the carbon/electrolyte contact and SEI formation) and high micropore volume (which is assumed to enhance capacity). Although the current paper is focused on carbon xerogels, considered here as model materials, the methodology could be further extended to other carbon-based electrode materials.

In order to develop further CXs and CVD-coated CXs toward high capacity electrode materials, both the internal carbon structure, including open/closed porosities and graphene layer stacking/disorder, and the Na^+ insertion-deinsertion mechanisms, should be investigated. In that respect, Small Angle X-ray Scattering (SAXS) could provide further insight on the carbon inner structure and the impact of the various post-treatments on the micropores, even though data analysis on such samples still cannot be considered as routine and, in our opinion, needs specific development. Nuclear Magnetic Resonance (NMR) is an interesting option to further understand the Na^+ insertion-deinsertion mechanisms, which could then be related to the fine analysis of the carbon structure. Further studies should definitely be focused on those topics."

Acknowledgements

N.J. and B.K. would like to thank the F.R.S-FNRS for providing funding as part a PDR project (Convention T.0142.20). D.H. and R.J. acknowledge the ANR – FRANCE (French National Research Agency) for its financial support of the OSES project (ANR-22-CE05-0003-01). A.F.L. thanks the University of Liège (Fonds Spéciaux pour la Recherche FSR) and the Fonds de Bay for their financial supports. UL authors gratefully acknowledge TALiSMAN and TALiSMAN2 projects, funded by the European Regional Development Fund (ERDF).

5. References

[1] B.E. Lebrouhi, S. Baghi, B. Lamrani, E. Schall, T. Kousksou, *J Energy Storage* **2022**, *55*, 105471.

[2] J.F. Peters, M. Baumann, B. Zimmermann, J. Braun, M. Weil, *Renew Sustain Energy Rev* **2017**, *67*, 491.

[3] H. Zhang, Y. Huang, H. Ming, G. Cao, W. Zhang, J. Ming, R. Chen, *J Mater Chem A Mater* **2020**, *8*, 1604.

[4] T. Perveen, M. Siddiq, N. Shahzad, R. Ihsan, A. Ahmad, M.I. Shahzad, *Renew Sustain Energy Rev* **2020**, *119*, 109549.

[5] K. Chayambuka, G. Mulder, D.L. Danilov, P.H.L. Notten, *Adv Energy Mater* **2020**, *10*, 38.

[6] P. Ge, M. Fouletier, *Solid State Ion* **1988**, *28–30*, 1172.

[7] D.A. Stevens, J.R. Dahn, *J Electrochem Soc* **2001**, *148*, A803.

[8] C. Bommier, T.W. Surta, M. Dolgos, X. Ji, *Nano Lett* **2015**, *15*, 5888.

[9] D. Saurel, B. Orayech, B. Xiao, D. Carriazo, X. Li, T. Rojo, *Adv Energy Mater* **2018**, *8*, 1703268.

[10] L.F. Zhao, Z. Hu, W.H. Lai, Y. Tao, J. Peng, Z.C. Miao, Y.X. Wang, S.L. Chou, H.K. Liu, S.X. Dou, *Adv Energy Mater* **2021**, *11*, 2002704.

[11] N. Cuesta, I. Cameán, A. Arenillas, A.B. García, *Micropor. Mesopor. Mater* **2020**, *308*, 110542.

[12] R. Dong, F. Wu, Y. Bai, Q. Li, X. Yu, Y. Li, Q. Ni, C. Wu, *Energy Mater Adv* **2022**, 9896218.

[13] X. Feng X, F.Wu ,Y. Fu ,Y. Li,Y. Gong, X. Ma, P. Zhang, C. Wu, Y. Bai, *Small* **2024**, *21*, 2409120.

[14] M. Liu, F. Wu, Y. Gong, Y. Li, Y. Li, X. Feng, Q. Li, C. Wu, Y. Bai, *Adv Mater* **2023**, *35*, 2300002.

[15] C. Bommier, W. Luo, W.Y. Gao, A. Greaney, S. Ma, X. Ji, *Carbon* **2014**, *76*, 165.

[16] B. Karaman, H. Tonnoir, D. Huo, B. Carré, A.F. Léonard, J.C. Gutiérrez, M.L. Piedboeuf, A. Celzard, V. Fierro, C. Davoisne, R. Janot, N. Job, *Carbon* **2024**, *225*, 119077.

[17] D.A. Stevens, J.R. Dahn, *J. Electrochem. Soc.* **2001**, *148*, A803.

[18] J.M. Stratford, P.K. Allan, O. Pecher, P.A. Chater, C.P. Grey, *Chem Comm* **2016**, *52*, 12430.

[19] D.A. Stevens, J.R. Dahn, *J Electrochem Soc* **2000**, *147*, 1271.

[20] D.A. Stevens, J.R. Dahn, *J Electrochem Soc* **2000**, *147*, 4428.

[21] N. Job, R. Pirard, J. Marien, J.P. Pirard, *Carbon* **2004**, *42*, 619.

[22] C.A. Páez, M.S. Contreras, A. Léonard, S. Blacher, C.G. Olivera-Fuentes, J.P. Pirard, N. Job, *Adsorption* **2012**, *18*, 199.

[23] X. Zhao, P. Shi, H. Wang, Q. Meng, X. Qi, G. Ai, F. Xie, X. Rong, Y. Xiong, Y. Lu, Y.-S Hu, *Energy Storage Mater.*, **2024**, 70, 103543.

[24] W. Hou, L. Ma, Z. Liu, Y. Hu, W. Miao, B.Tao, K. Sun, H. Peng, G. Ma, *J. Energy Chem.*, **2025**, 105, 65-75.

[25] H. Zhang, J. Yin, D. Ouyang, Y. Liu, R. Wu, R. Zhang, R. Huo, G. Yang, Y. Cai, J. Yin, *J. Mater. Chem. A*, **2025**, 13, 8679–8690.

[26] N. Job, A. Théry, R. Pirard, J. Marien, L. Kocon, J.-N. Rouzaud, et al. *Carbon*, 2005, *43*, 2481-2494

[27] S. Brunauer, P.H. Emmett, E. Teller, *J Am Chem Soc* **1938,** *60*, 309.

[28] J. Rouquerol, P. Llewellyn, F. Rouquerol, *Stud Surf Sci Catal* **2007,** *160*, 49.

[29] Washburn, Edward W. *Physical review* **1921**, *17.3*, 273.

[30] P. Mallet-Ladeira, PhD Thesis, Université de Toulouse 3 Paul Sabatier, **2014**. France.

[31] M.L. Piedboeuf, A. F. Léonard, C. Balzers, G. Reichenauer, N. Job. *Micropor. Mesopor. Mater*, **2019**, *275*, 278-287

[32] B. Ranjan, D. Kaur, *Small* **2024**, *20*, 2307723.

[33] P.J.F. Harris, *Crit. Rev. Solid State Mater Sci.* **2005**, *30*, 235.

[34] P.J.F. Harris, A. Burian, S. Duber, *Philos Mag Lett* **2000**, *80*, 381.

[35] J. Ren, H. Weng, B. Li, F Chen, J. Liu, Z. Song. *Front Earth Sci*. **2022**, *10*, 841353

[36] B. Sajjadi, W.-Y. Chen, N. O. Egiebor, *Rev Chem Eng*, **2019**, *35(7)*, 777–815

[37] C. del Mar Saavedra Rios, A. Beda, L. Simonin, C.M. Ghimbeu, In: Na-Ion Batteries (Eds. L. Monconduit and L. Croguennec), Wiley, **2021**, ISBN 978-1-789-45013-2, Ch. 3, p.101.

[38] A. Arenillas, J. A. Menéndez, G. Reichenauer, A. Celzard, V. Fierro, F.José M. Hodar, E.Bailón-Garcia, N. Job, Carbon Gels for Electrochemical Applications. In: Organic and Carbon Gels. Advances in Sol-Gel Derived Materials and Technologies. Springer, **2019**, Ch. 5, p. 149.

[39] S. Kumar, E. Majhi, A. S. Deshpande M. Khandelwal, *Carbon Trends,* **2024,** *16*, 100385.

[40] R. Tang, K. Nomura, K. Inoue, M. Kotani, T. Kyotani, H. Nishihara, *Electrochim. Acta*, **2022**, 429, 141009.

[41] M. L. Piedboeuf, N. Job, A. Aqil, Y. Busby, V. Fierro, A. Celzard, C. Detrembleur, A.F. Léonard, *ACS Appl Mater Interfaces* **2020**, *12*, 36054.

[42] H. Zheng, J. Li, X. Song, G. Liu, V.S. Battaglia, *Electrochim Acta* **2012**, *71*, 258.

[43] R. Zhao, J. Liu, J. Gu, *Appl Energy* **2015**, *139*, 220.

[44] B. Yang, S. Liu, H. Song, J. Zhou, *Carbon* **2019**, *153*, 298.